ACS APPLIED MATERIALS & INTERFACES

Research Article

www.acsami.org

Superior Performance Asymmetric Supercapacitors Based on a Directly Grown Commercial Mass 3D Co_3O_4@$Ni(OH)_2$ Core–Shell Electrode

Chun-hua Tang, Xuesong Yin, and Hao Gong*

Department of Materials Science and Engineering, National University of Singapore, 117576 Singapore

Supporting Information

ABSTRACT: Pseudocapacitors based on fast surface Faradaic reactions can achieve high energy densities together with high power densities. Usually, researchers develop a thin layer of active materials to increase the energy density by enhancing the surface area; meanwhile, this sacrifices the mass loading. In this work, we developed a novel 3D core–shell Co_3O_4@$Ni(OH)_2$ electrode that can provide high energy density with very high mass loading. Core–shell porous nanowires (Co_3O_4@$Ni(OH)_2$) were directly grown on a Ni current collector as an integrated electrode/collector for the supercapacitor anode. This Co_3O_4@$Ni(OH)_2$ core–shell nanoarchitectured electrode exhibits an ultrahigh areal capacitance of 15.83 F cm^{-2}. The asymmetric supercapacitor prototypes, assembled using Co_3O_4@$Ni(OH)_2$ as the anode, reduced graphene oxide (RGO) or active carbon (AC) as the cathode, and 6 M aqueous KOH as the electrolyte, exhibit very high energy densities falling into the energy-density range of Li-ion batteries. Because of the large mass loading and high energy density, the prototypes can drive a minifan or light a bulb even though the size is very small. These results indicate that our asymmetric supercapacitors have outstanding potential in commercial applications. Systematic study and scientific understanding were carried out.

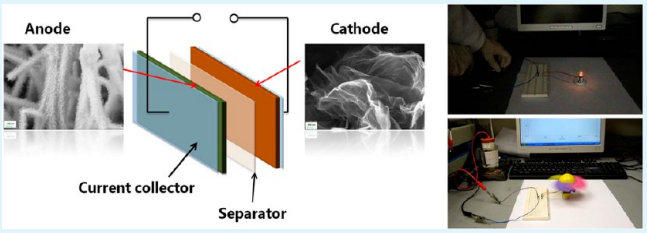

KEYWORDS: *asymmetric supercapacitors, nickel hydroxide, cobalt oxide, core–shell nanostructure*

1. INTRODUCTION

Energy crisis, caused by over usage of fossil-fuel resources and environmental pollution, is one of the crucial problems facing society today. Therefore, electric-energy-storage devices with a high energy-storage capacity and fast charge ability are very desirable.[1−3] Supercapacitors, also known as electrochemical capacitors, are suitable for many applications that require a high energy density and fast charge–discharge rate, such as hybrid electric vehicles and industrial equipment.[4,5]

Currently, most commercial supercapacitors are carbon-based symmetric devices, usually with a specific areal capacitance (C_a) of about (10−50) × 10^{-6} F cm^{-2} and an energy density of 3 to 4 Wh kg^{-1} (at a power density of 3 to 4 kW kg^{-1}) in both aqueous electrolyte and organic electrolyte.[2,6,7] Although this energy density is suitable for many applications, it is far below the 30−200 Wh kg^{-1} of Li-ion batteries.[8] To obtain a higher capacitance and energy density compared to carbon materials, transition-metal oxide/hydroxide is a good choice for use in supercapacitor applications because they can store more charge and energy via Faradic reaction.[4,9−11] Besides the various merits of metal oxide/hydroxide,[6−8] nanostructured transition-metal oxide/hydroxide has the ability to facilitate interfacial electrochemical reactions because of a large surface area. Many 3D hybrid nanostructure metal oxides, such as NiO-TiO_2 nanotube arrays,[12] Co_3O_4@MnO_2[13] core–shell nanowires, and ZnO@MoO[14] core–shell structures, have been researched to replace RuO_x, which has good pseudocapacitive behavior but limited applications because of its rarity and high cost. Among different nanostructures, a 3D structure is promising for enhancing electrochemical behaviors because of the short ion-diffusion path and enlarged surface area that provides more efficient contacts between the electrolyte ions and active materials for Faradaic energy storage.[15] Meanwhile, the direct growth of nanoarrays on conductive substrates can facilitate the diffusion of active species and the transport of electrons[16−18] as well as avoid utilizing additives that can increase supercapacitor resistance. Unfortunately, achieving a high mass loading without the use of binder additives on a current collector is a major challenge that limits the areal capacitance that is crucial for supercapacitors. For instance, it was reported that a Co_3O_4@NiO[19] core–shell nanowires structure had an areal capacitance of only 2.56 F cm^{-2}, even though it had a high gravimetric capacitance (857 F g^{-1}), because of the low areal mass loading. Therefore, in this work, we focus on fabricating 3D hybrid nanostructure pseudocapacitive electrodes with a very high mass loading.

Received: June 24, 2013
Accepted: October 3, 2013
Published: October 3, 2013

Another approach to enhance the energy density of a supercapacitor is to design an asymmetric supercapacitor full-cell setup. Asymmetric supercapacitors with energy densities higher than carbon-based symmetric supercapacitors were developed as potential energy-storage devices to increase the energy density.[20−22] These asymmetric supercapacitors consist of a nonpolarized Faradaic electrode (as the energy source) and a polarized electrode (as the power source).[23,24] Therefore, such supercapacitors not only retain the behaviors of the supercapacitors, such as high charging−discharging rate and long cycle life, but also provide a high energy density, approaching that of a battery.[6,25] By considering the practical applications of nanostructured electrodes, asymmetric supercapacitors were developed in this work.

In this article, we report an additive-free, 3D nanoarchitectured Co_3O_4@$Ni(OH)_2$/NF (nickel foam) core−shell nanowire electrode with a commercially high mass loading (11.9 mg cm^{-2}). This core−shell nanowire electrode has a high areal capacitance up to around 15.83 F cm^{-2}, with a corresponding gravimetric capacitance of 1330.0 F g^{-1}. To the best of our knowledge, this areal capacitance is the best reported data for a hybrid metal-oxide system. On the basis of this Co_3O_4@$Ni(OH)_2$/NF electrode, asymmetric supercapacitors prototypes were developed using metal oxide@hydroxide as the anode and carbonaceous materials as the cathode. These asymmetric supercapacitors exhibited superior capacitances and energy densities. Because of the large mass loading and high energy densities, the asymmetric supercapacitors can supply power to run a 3 V minifan or to light a 2.5 V bulb even though the area is only 4 cm^2.

2. EXPERIMENTAL SECTION

2.1. Co_3O_4 Nanowire Synthesis. The Co_3O_4 nanowire array was synthesized using a hydrothermal method. $CoSO_4{\cdot}6H_2O$ (10 mmol), 20 mmol of NH_4F, and 50 mmol of urea were dissolved in 50 mL of water under constant stirring. After 10 min of stirring, a transparent homogeneous solution was obtained and transferred into Teflon-lined stainless steel autoclaves. A piece of clean nickel foam (2 × 2 cm^2) was immersed into the above aqueous solution. Next, the autoclave was sealed and heated at 120 °C for 5 h and then allowed to cool to room temperature spontaneously. After the reaction, the coated substrate was collected from the solution and then ultrasonicated in deionized water for 1 min to remove possible free nanoparticles and residual reactant. Finally, the coated substrate was calcinated at 250 °C in air for 4 h, and the as-synthesized Co_3O_4 nanowire array grown on the substrate was obtained.

2.2. Core−Shell Nanowires Synthesis. To grow $Ni(OH)_2$ shells on Co_3O_4 nanowire cores, a solution was prepared by mixing 40 mL of 1M $NiSO_4{\cdot}6H_2O$, 30 mL of 0.25M $K_2S_2O_4$, 10 mL of aqueous ammonia (24% $NH_3{\cdot}H_2O$), and 20 mL of deionized water in a 250 mL Pyrex beaker at room temperature. The Co_3O_4-coated Ni foam (Co_3O_4/NF) was immersed into the aqueous solution. When the room temperature chemical-bath deposition of $Ni(OH)_2$ was performed for 15 min, the $Ni(OH)_2$-coated Co_3O_4/NF (Co_3O_4@$Ni(OH)_2$/NF) electrode/collector sample was subjected to a high-speed rotation rinsing at 500 rpm for 3 min. Then, the sample was dried at 120 °C for 12 h.

2.3. Cathode Electrode Fabrication. The reduced graphene oxide (RGO)- or AC-based cathode was prepared by mixing 90 wt % reduced graphene oxide (high porous reduced graphene oxide, Graphene Supermarket) or activated carbon (Black Pearl 2000, Cabot) and 10 wt % PTFE and spreading the mixture paste onto a 2 × 2 cm^2 Ni foam. Then, the electrode was dried at 70 °C in air for 2 h, pressed at 8 MPa, and kept at 120 °C in air for 12 h.

2.4. Material Characterization. The morphology and microstructure of the synthesized samples were characterized using scanning electron microscopy (SEM, Zeiss) and transmission electron microscopy (TEM, JEOL 2010) with an energy-dispersive X-ray (EDS) analyzer. Specific surface area and pore volume for the samples of the active-materials-coated Ni foams were measured by a nitrogen adsorption−desorption system (Micromeritics ASAP2020) using the Brunauer−Emmet−Tell (BET) and Barrett−Joyner−Halenda (BJH) method. The X-ray diffraction (XRD) patterns of the samples were obtained with Bruker AXS (D8 Advance, Cu Kα, λ = 0.154060 nm) at 40 kV and 40 mA . Electrochemical measurements of a single electrode were carried out in a three-electrode arrangement with the as-prepared electrode as the working electrode, a platinum plate as the counter electrode, and a saturated calomel electrode (SCE) as the reference electrode, in 6 M KOH electrolyte. Electrochemical performance was evaluated by cyclic voltammetry (CV) and galvanostatic charge−discharge tests (Solartron SI 1287). The weight of a sample was measured using a Mettler Toledo X205DU microbalance (sensitivity, 0.01 mg; repeatability, 0.015 mg). Before weighing, all of the samples were dried in an oven at 120 °C for at least 2 days. The mass loading of the active materials was calculated by $m_2 - m_1$, where m_1 is the mass of the Ni foam and m_2 is the mass of the Ni foam coated with the active materials.

2.5. Assembly of the Asymmetric Supercapacitor. An asymmetric supercapacitor was assembled with an integrated Co_3O_4@$Ni(OH)_2$/NF anode/collector, an RGO (or AC)/NF cathode/collector, and 6 M KOH electrolyte. A series of electrochemical tests, including cyclic voltammetry (CV) and galvanostatic charge−discharge measurements for an asymmetric supercapacitor, was performed with a Solartron Electrochemical System SI 1287.

3. RESULTS AND DISCUSSION

3.1. Fabrication and Characterization of Co_3O_4@$Ni(OH)_2$ Core−Shell Electrodes. The two-step synthesis process of the Co_3O_4@$Ni(OH)_2$ core−shell electrode, which combines hydrothermal growth and chemical-bath deposition, is illustrated in Figure S1a. The Co_3O_4 nanowire array, directly grown on the nickel foam (NF) by a hydrothermal method, serves as the core for the further deposition of the $Ni(OH)_2$ shell. Figure S1b shows a photograph of a pristine NF, the integrated $Co_2(CO_3)(OH)_2$/NF, Co_3O_4/NF, and Co_3O_4@$Ni(OH)_2$/NF electrode/collector assemblies, respectively. A high-coverage growth of Co_3O_4 nanowires on the porous nickel foams was observed, and the silver color NF turned black. After the chemical-bath deposition of $Ni(OH)_2$ shells, the Co_3O_4/NF was covered by a light-green lamella, which indicated the formation of the $Ni(OH)_2$ onto the Co_3O_4/NF.

XRD patterns of the Co_3O_4/NF and the Co_3O_4@$Ni(OH)_2$/NF nanowire electrodes are shown in Figure 1. The diffraction peaks for the sample of Co_3O_4/NF belong to Co_3O_4 (JCPDS no. 42-1467) and Ni (JCPDS no. 01-1258). The three highest intensity peaks at 44.4°, 51.6°, and 76.1° belong to (111), (200), and (220) of metallic nickel, respectively. The peaks positioned at 31.3°, 36.9°, 59.4°, and 65.2° in both patterns belong to (220), (311), (511), and (440) of Co_3O_4, respectively. In the XRD pattern of Co_3O_4@$Ni(OH)_2$/NF, additional peaks are observed at 11.6°, 23.8°, 33.7°, and 59.6°, which belong to (001), (002), (110), and (300) of α-$Ni(OH)_2$ (JCPDS no. 22-0444), respectively. Therefore, the results prove that the surface of the Co_3O_4 nanowire was decorated with $Ni(OH)_2$.

Figure 2 shows the morphologies of the pristine Ni foam, $Ni(OH)_2$/NF, Co_3O_4/NF, and Co_3O_4@$Ni(OH)_2$/NF. As shown in Figure 2a, the commercial nickel foam has a 3D structure with a relatively plain surface. The 3D structure can provide more surface area to allow more active materials to grow on it. After the $Ni(OH)_2$ chemical-bath deposition,

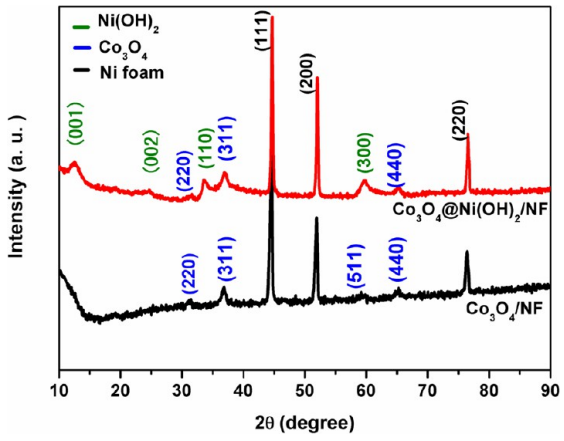

Figure 1. XRD patterns of the Co_3O_4/NF and Co_3O_4@$Ni(OH)_2$/NF nanowire electrodes.

$Ni(OH)_2$ nanowalls directly grew on the nickel foam (Figure 2b); meanwhile, $Ni(OH)_2$ nanospheres can assemble on some of the edges of the nickel foam (Figure 2b inset). However, the coverage is very poor, and the mass of $Ni(OH)_2$ on the nickel foam is measured to be only 0.25 mg cm^{-2}. After a blank nickel foam underwent a hydrothermal growth of Co_3O_4 nanowires, its surface became rougher because of the coverage of a layer of 3D Co_3O_4 nanowire arrays (Figure 2c). After the $Ni(OH)_2$ was deposited on the Co_3O_4/NF structure, the surface of the Co_3O_4 nanowires was decorated with $Ni(OH)_2$ nanoflakes. From the low-magnification SEM images (Figure 2d), there is a very high coverage of the coating, and the loading of $Ni(OH)_2$ increased greatly compared with that seen in Figure 2b. In the Co_3O_4@$Ni(OH)_2$/NF electrode, the mass of the 2 × 2 cm^2 pristine Ni foam was 0.1721 g (i.e., 43.03 mg cm^{-2}). After the growth of the Co_3O_4 nanowires, the mass became 0.1914 g (i.e., 47.85 mg cm^{-2}), whereas after a further growth of $Ni(OH)_2$ the mass became 0.2197 g (i.e., 54.93 mg cm^{-2}). Therefore, the mass of the $Ni(OH)_2$ was 7.08 mg cm^{-2}, the mass of Co_3O_4 was 4.8 mg cm^{-2}, and the mass of Co_3O_4 plus $Ni(OH)_2$ was 11.88 mg cm^{-2}. The 7.08 mg cm^{-2} mass of $Ni(OH)_2$ on Co_3O_4/NF is 28 times higher than that of $Ni(OH)_2$ directly grown on a pristine nickel foam (Table 2). The enhancement of $Ni(OH)_2$ mass loading was due to a high coverage of $Ni(OH)_2$ nanoflakes on 3D porous Co_3O_4 nanowire arrays grown on nickel foam.

Table 1 lists the BET surface area and BJH desorption cumulative pore volume results of the NF, $Ni(OH)_2$/NF, Co_3O_4/NF, and Co_3O_4@$Ni(OH)_2$/NF electrodes. The BJH desorption cumulative pore volume is calculated on the basis of the pores with sizes from 1.7 to 300 nm. For $Ni(OH)_2$ directly grown on NF, the BET surface area is 0.37 m^2 g^{-1}, just slightly

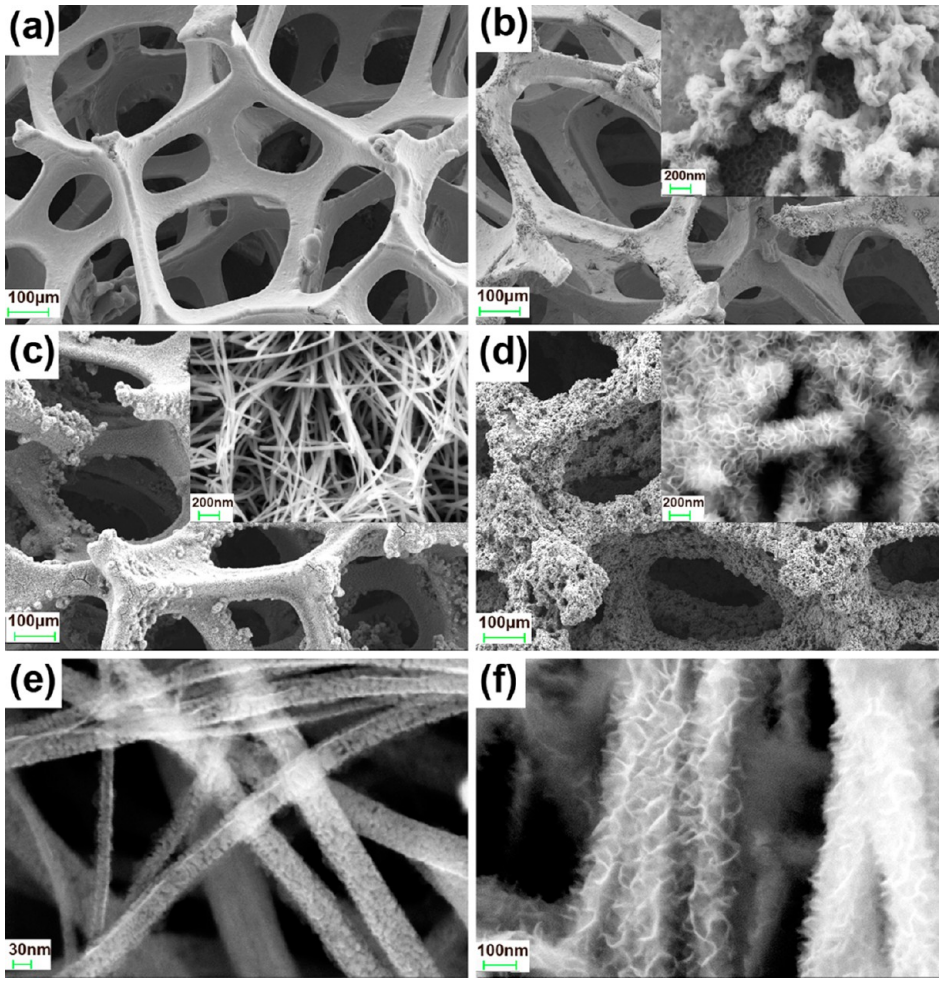

Figure 2. SEM images of blank Ni foam (a), $Ni(OH)_2$ directly grown on Ni foam without Co_3O_4 nanowire arrays (b), Co_3O_4/NF (c), Co_3O_4@$Ni(OH)_2$/NF (d). High-magnification SEM images of Co_3O_4/NF (e) and Co_3O_4@$Ni(OH)_2$/NF (f).

Table 1. BET Surface Area and BJH Desorption Cumulative Pore Volume of Ni Foam (NF), $Ni(OH)_2$/NF, Co_3O_4/NF, and Co_3O_4@$Ni(OH)_2$/NF

	BET surface area (m^2 g^{-1})	BJH desorption cumulative pore volume (cm^3 g^{-1})
NF	0.33	0.00036
$Ni(OH)_2$/NF	0.37	0.00158
Co_3O_4/NF	14.74	0.05020
Co_3O_4@ $Ni(OH)_2$/NF	10.30	0.04395

higher than 0.33 m^2 g^{-1} of the NF, because of a poor coverage of $Ni(OH)_2$ on the NF surface (Figure 2b, SEM image). A tremendous increase in surface area and pore volume was observed after the hydrothermal growth of Co_3O_4 nanowires on nickel foams. The BET surface area increased from 0.33 to 14.74 m^2 g^{-1} with an enhancement in BJH pore volume from 0.00036 to 0.0502 cm^3 g^{-1}; after that, the NF was coated with Co_3O_4, in agreement with the SEM observation. After the deposition of $Ni(OH)_2$ on Co_3O_4/NF, the BET surface area and BJH pore volume had a slight drop compared with Co_3O_4/NF (Table 1) because some pores on the Co_3O_4 nanowires were filled by $Ni(OH)_2$ nanoflakes. The improvement of surface area and pore volume accompanied by a significant increase in the loading of active materials can be significant in enhancing the capacitive performance, especially in raising the areal pseudocapacitance. Co_3O_4 nanowires (4.83 mg cm^{-2}) was deposited on nickel foam after hydrothermal synthesis, and Co_3O_4 is also a pseudocapacitive candidate that contributes to the capacitive performance. The capacitive performance will be discussed later. From the high-magnification SEM images (Figure 2e,f) we can observe the following: (1) the Co_3O_4 nanowire has lots of pores on its surface and (2) $Ni(OH)_2$ nanoflakes fully cover the Co_3O_4 nanowires to form a 3D core−shell structure. The 3D core−shell nanowire structure is favorable for the electrode applications of pseudocapacitors because the surface area becomes very large and the interconnected pores form channels that allow the electrolyte to diffuse easily.

The structural and morphological properties of the Co_3O_4 nanowire and Co_3O_4@$Ni(OH)_2$ core−shell were characterized by transmission electron microscopy (TEM), as shown in Figure 3. Figure 3a,d show the typical TEM images of an individual Co_3O_4 nanowire and a Co_3O_4@$Ni(OH)_2$ core−shell structure. From these images and from Figure 2e, the Co_3O_4 porous nanowires had diameters of around 20−70 nm. In Figure 3d, the hybrid core−shell nanowire shows the gauzelike $Ni(OH)_2$ nanosheets fully covering the Co_3O_4 nanowire core. The bright dots in the selected-area electron diffraction (SAED) pattern of the Co_3O_4 nanowire (Figure 3b) indicated that the nanowire is a single crystal. The characteristic bright dots in the diffraction pattern of the Co_3O_4 nanowire can be indexed as (220), (440), (311), (400), and (511) of the cubic structure Co_3O_4 (JCPDS no. 42-1467), respectively, as shown in Figure 3b. The lattice of Co_3O_4 can also be observed in the HR-TEM image of the Co_3O_4 nanowire (Figure 3c). The SAED pattern of the Co_3O_4@$Ni(OH)_2$ core−shell nanowire in Figure 3e was composed of not only bright dots but also rings. The rings in the diffraction pattern can be indexed as the (111), (103), and (300) of α-$Ni(OH)_2$ (JCPDS no. 22-0444), respectively, as shown in Figure 3e, in agreement with our previous work.[26] The Co_3O_4@$Ni(OH)_2$ core−shell nanowire was unambiguously confirmed by energy-dispersive X-ray spectrometry (EDS) mapping analysis shown in Figure 3f. The mapping analysis indicated that the inner nanowire core was Co_3O_4 and the outer-layer shell was $Ni(OH)_2$ in the hybrid core−shell structure.

3.2. Electrochemical Characterization of the Co_3O_4@$Ni(OH)_2$/NF Electrode. The electrochemical behaviors of the Co_3O_4@$Ni(OH)_2$/NF electrode were evaluated by cyclic voltammetry (CV) and galvanostatic charge−discharge measurement in a three-electrode system with a 6 M KOH aqueous

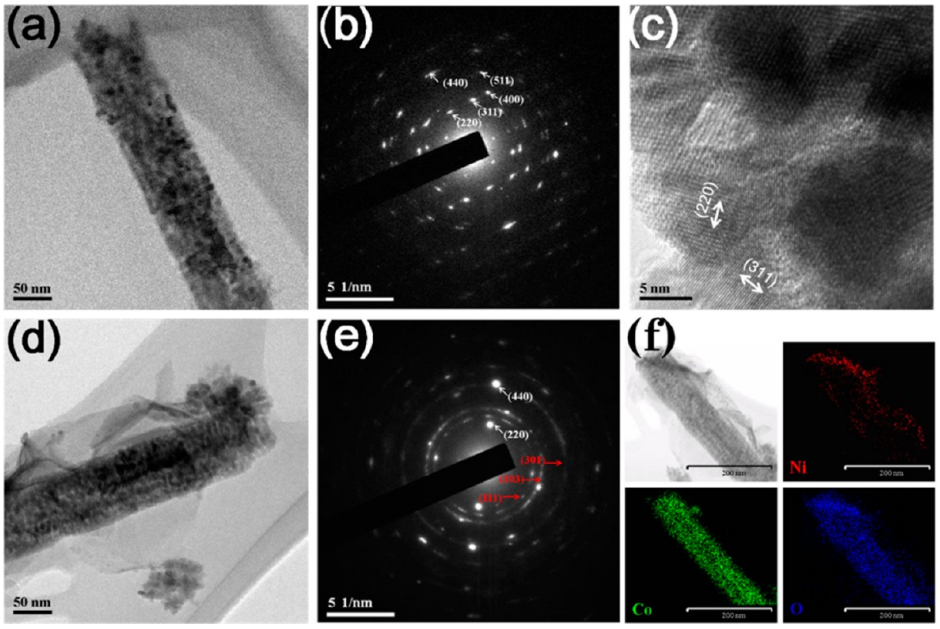

Figure 3. TEM images of a single Co_3O_4 nanowire (a) and Co_3O_4@$Ni(OH)_2$ (d). SAED patterns of a single Co_3O_4 nanowire (b) and Co_3O_4@$Ni(OH)_2$ (e). High-resolution TEM image of a single Co_3O_4 nanowire (c). EDS elemental mapping images of the Co_3O_4@$Ni(OH)_2$ shell structure (f).

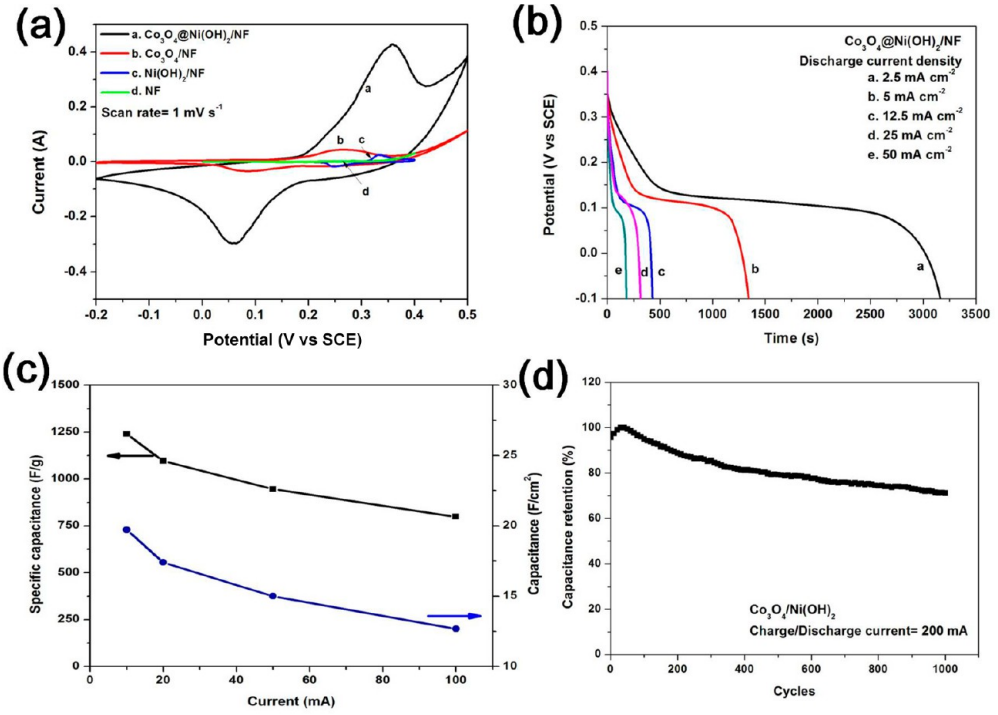

Figure 4. CV curves of the Co_3O_4@Ni(OH)$_2$/NF, Ni(OH)$_2$/NF, and Co_3O_4/NF electrodes and the pristine Ni foam (a). Discharge behavior of the Co_3O_4@Ni(OH)$_2$/NF electrode at different current densities (b). Current dependence of the areal capacitance (lower) and specific capacitance (upper) of the Co_3O_4@Ni(OH)$_2$/NF electrode (c). Capacitance retention of the Co_3O_4@Ni(OH)$_2$/NF electrode at a charge−discharge current of 200 mA for 1000 cycles (d).

electrolyte. Figure 4a shows the cyclic voltammograms (CVs) of a Co_3O_4@Ni(OH)$_2$/NF electrode and a Co_3O_4/NF electrode with a potential window between −0.2 and 0.5 V (vs SCE) and of a Ni(OH)$_2$/NF electrode and Ni foam with a potential window of 0−0.4 V (vs SCE) at a scan rate of 1 mV/s. As shown in Figure 4a, redox peaks exist in all of the CV curves. If we compare the CV curve of the nickel foam with that of the other three electrodes, then it is obvious that the contribution from the nickel foam to the capacitance value is very small, which can be ignored. The electrochemical reaction of the Ni(OH)$_2$/NF electrode in the KOH electrolyte is known to follow $Ni(OH)_2 + OH^- \rightarrow NiOOH + H_2O$, which involves the intercalation and deintercalation of protons. It can be noticed that the enclosed CV curve area and the potential window of the Ni(OH)$_2$/NF electrode are much smaller than those of the Co_3O_4/NF and Co_3O_4@Ni(OH)$_2$/NF electrodes. The narrower potential window is attributed to the intrinsic electrochemical property of Ni(OH)$_2$. The small enclosed area, reflecting the lower capacitance, was due to a low mass loading of Ni(OH)$_2$ (0.25 mg cm^{-2}) when being directly grown on NF. This mass loading is very small compared with 5.1 mg cm^{-2} Co_3O_4 of the Co_3O_4/NF sample and 11.9 mg cm^{-2} (4.82 mg cm^{-2} Co_3O_4 + 7.08 mg cm^{-2} Ni(OH)$_2$) of the Co_3O_4@Ni(OH)$_2$/NF sample. As we know, the total capacitance value of the electrode equals to the product of the mass of the active materials and the gravimetric capacitance. Even though the specific gravimetric capacitance of the Ni(OH)$_2$/NF was quite high (2820 F g^{-1}), the small mass loading led to a small total capacitance. We now compare the behavior of Co_3O_4@Ni(OH)$_2$/NF and Co_3O_4/NF. The redox peaks in the CV curve of the Co_3O_4/NF nanowire electrode are due to the reversible redox reaction of Co^{3+}/Co^{4+} associated with OH^- anions.[27] The redox peaks of Co_3O_4@Ni(OH)$_2$/NF are mainly contributed by the reversible redox reaction of Ni^{2+}/Ni^{3+} associated with anions OH^-, which occurs at the Ni(OH)$_2$ outer-layer shell.[28] A comparison of the CV curves of the Co_3O_4@Ni(OH)$_2$/NF and Co_3O_4/NF electrodes reveals the prominent contribution of the hybrid Co_3O_4@Ni(OH)$_2$/NF after comparing the areas enclosed by the CV curves. The area of the CV curve of the hybrid Co_3O_4@Ni(OH)$_2$/NF is much larger. It is obvious that the capacitance of the Co_3O_4@Ni(OH)$_2$ core−shell structure electrode is much higher than that of the Co_3O_4 nanowires electrode. The existence of 3D Co_3O_4 naowire arrays on the nickel foam allowed the growth of a vast amount of Ni(OH)$_2$ nanoflakes, leading to a boost in the capacitance value. Meanwhile, Co_3O_4 can also make some contribution to the pseudocapacitive, which is another advantage of using Co_3O_4 nanowires as the cores for Ni(OH)$_2$ shells.

To evaluate further the performance of the Co_3O_4@Ni(OH)$_2$/NF core−shell electrode, a series of charge−discharge measurements were performed at various charge−discharge currents of 10, 20, 50, 100, and 200 mA (corresponding to current densities of 2.5, 5, 12.5, 25, and 50 mA cm^{-2}, respectively) between −0.1 to 0.4 V. The charge−discharge curves of Co_3O_4/NF and Co_3O_4@Ni(OH)$_2$/NF are provided in the Supporting Information (Figures S3 and S4). The discharge curves are shown in Figure 4b. The discharge curves of the Co_3O_4@Ni(OH)$_2$/NF exhibited a typical pseudocapacitance behavior that is consistent with their CV results. The specific capacitances are calculated as

$$C_g = It/m\Delta V \quad (1)$$

and the area-normalized capacitances are calculated as

$$C_a = It/S\Delta V \quad (2)$$

where I (A) is the discharge current, m (g) is the mass of the core−shell structure, S (cm^2) is the geometrical area of the electrode, V (V) is the potential window, t (s) is the discharge time, and C_g and C_a (F g^{-1} or F cm^{-2}) are the specific gravimetric and areal capacitances, respectively. The gravimetric capacitance and areal capacitance values of the Co_3O_4@$Ni(OH)_2$/NF are illustrated in Figure 4c. The highest areal capacitance achieved by measuring the Co_3O_4@$Ni(OH)_2$/NF electrode is 15.83 F cm^{-2} (corresponding to a specific gravimetric capacitance of 1330.0 F g^{-1}) at a current density of 2.5 mA cm^{-2}. To the best of our knowledge, this areal capacitance value is the highest among the reported studies of supercapacitor electrodes. This great enhancement in the areal capacitance is not only contributed by the good pseudocapacitive candidate materials such as Co_3O_4 and $Ni(OH)_2$ but also by the high mass loading of active materials because of the special core−shell structure. Table 2 compares our Co_3O_4@$Ni(OH)_2$/NF electrode with literature-reported $Ni(OH)_2$-based and different core−shell electrodes. The 1330.0 F g^{-1} gravimetric capacitance of our Co_3O_4@$Ni(OH)_2$/NF electrode is higher than the values of Co_3O_4@MnO_2 coreshell arrays (480 F g^{-1}),[13] CoO@NiHON hybrid structures (798.3 F g^{-1}),[29] and ordered NiO-TiO_2 nanotube arrays (40−100 F g^{-1}).[12] These results suggested that our binder-free Co_3O_4@$Ni(OH)_2$/NF electrode has excellent pseudocapacitive behavior. The highly porous crystalline core material (seen in SAED images) is directly grown on the NF current collector. This direct contact can assure quick electron transport to improve the capacitance performance.[30] This high performance could also be attributed to the electrode structrure of single-crystalline Co_3O_4 porous nanowire cores and ultrathin polycrystalline $Ni(OH)_2$ nanoflake shells. The existence of porous Co_3O_4 nanowires leads to a much higher loading of $Ni(OH)_2$ on the current collector as compared to the pristine Ni foam (see the SEM images). The areal capacitance of this electrode increased with an increase in the loading of $Ni(OH)_2$. The cycling life of the Co_3O_4@$Ni(OH)_2$/NF electrode was further investigated by performing the galvanostatic charge−discharge cycling between −0.1 and 0.4 V at a high current of 200 mA (i.e., 50 mA cm^{-2}). One thousand cycles were continuously performed, and the relative specific capacitance variation of the Co_3O_4@$Ni(OH)_2$/NF electrode along with the cycle number is shown in Figure 4d. The capacitance of the electrode increased in the initial several cycles, in agreement with literature,[11] because of the activation of the active materials. A total capacitance loss of 24% from the initial value was observed after the electrode was tested for 1000 cycles. This was probably due to the loosening of the active materials from the nickel foam because the electrolyte became blue after measurement. Compared with the 48% capacitance loss of the $Ni(OH)_2$-based electrode after 300 cycles, as reported previously,[31] our core−shell electrode demonstrates a good cycling performance after 1000 cycles at a high charge−discharge rate.

Table 2. Areal Mass Loading and Specifc Capacitance of Co_3O_4@$Ni(OH)_2$/NF Compared with Other Different Electrodes Reported in Literature

electrode structure	gravimetric capacitance (F g^{-1})	areal mass loading (mg cm^{-2})	areal capacitance (F cm^{-2})
Co_3O_4@ $Ni(OH)_2$/ NF[a]	1330	11.90	15.83
$Ni(OH)_2$/NF[a]	2820	0.25	0.7
CNT@ $Ni(OH)_2$/ NF[26]	3300	4.85	16
$Ni(OH)_2$/NF[35]	2200	1.92	4.22
$Ni(OH)_2$/ USY/NF[31]	1740	3.35	5.83
Co_3O_4@ MnO_2/ITO[13]	480	1.56	0.75
Co_3O_4@NiO/ NF[19]	857	2.99	2.56

[a]These results are from this work.

3.3. Asymmetric Supercapacitors with a Co_3O_4@$Ni(OH)_2$/NF Anode and a RGO (or AC) Cathode. To evaluate the capacitive performance of a full-cell supercapacitor device employing the Co_3O_4@$Ni(OH)_2$/NF electrode, we developed Co_3O_4@$Ni(OH)_2$/NF-based asymmetric supercapacitor prototypes. As shown in Figure 5a, the Co_3O_4@$Ni(OH)_2$/NF electrode was used as the positive electrode and a RGO- (reduced graphene oxide) or AC-based (active carbon) electrode was used as the negative electrode. The information on the electrochemical property of the RGO- and AC-based single electrode is provided in the Supporting Information (Figures S6 and S7). The specific capacitances of the RGO- and AC-based single electrodes were measured to be 182 and 120 F g^{-1}, respectively. In both of these two types of asymmetric supercapacitors, the mass ratio of the anode and cathode active materials is 1:3.7, close to the theoretical mass ratio (1:3 to 1:4) in obtaining an optimized energy density proposed by Zheng[32]. These two asymmetric supercapacitors using RGO and AC cathodes were labeled as Co_3O_4@$Ni(OH)_2$//RGO and Co_3O_4@$Ni(OH)_2$//AC for convenience, respectively. Figure 5b,c show that after fast charging the Co_3O_4@$Ni(OH)_2$//RGO asymmetric supercapacitor can practically be utilized as the power supply for a minifan and a bulb even though the dimension of this supercapacitor is very small (only 4 cm^2). These results demonstrate that our asymmetric supercapacitor prototypes have outstanding potential for use in practical applications.

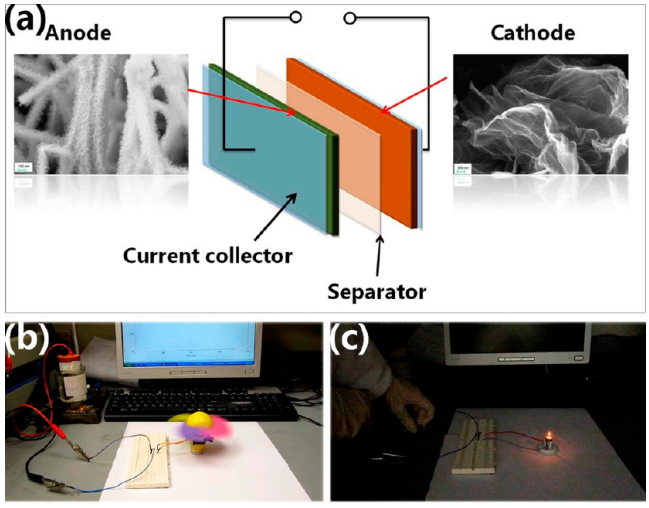

Figure 5. Schematic illustration of the fabricated Co_3O_4@$Ni(OH)_2$//RGO asymmetric supercapacitor prototype in 6 M KOH electrolyte (a). Photographs of the Co_3O_4@$Ni(OH)_2$//RGO asymmetric supercapacitor prototype as a power supply for a minifan (b) and a bulb (c).

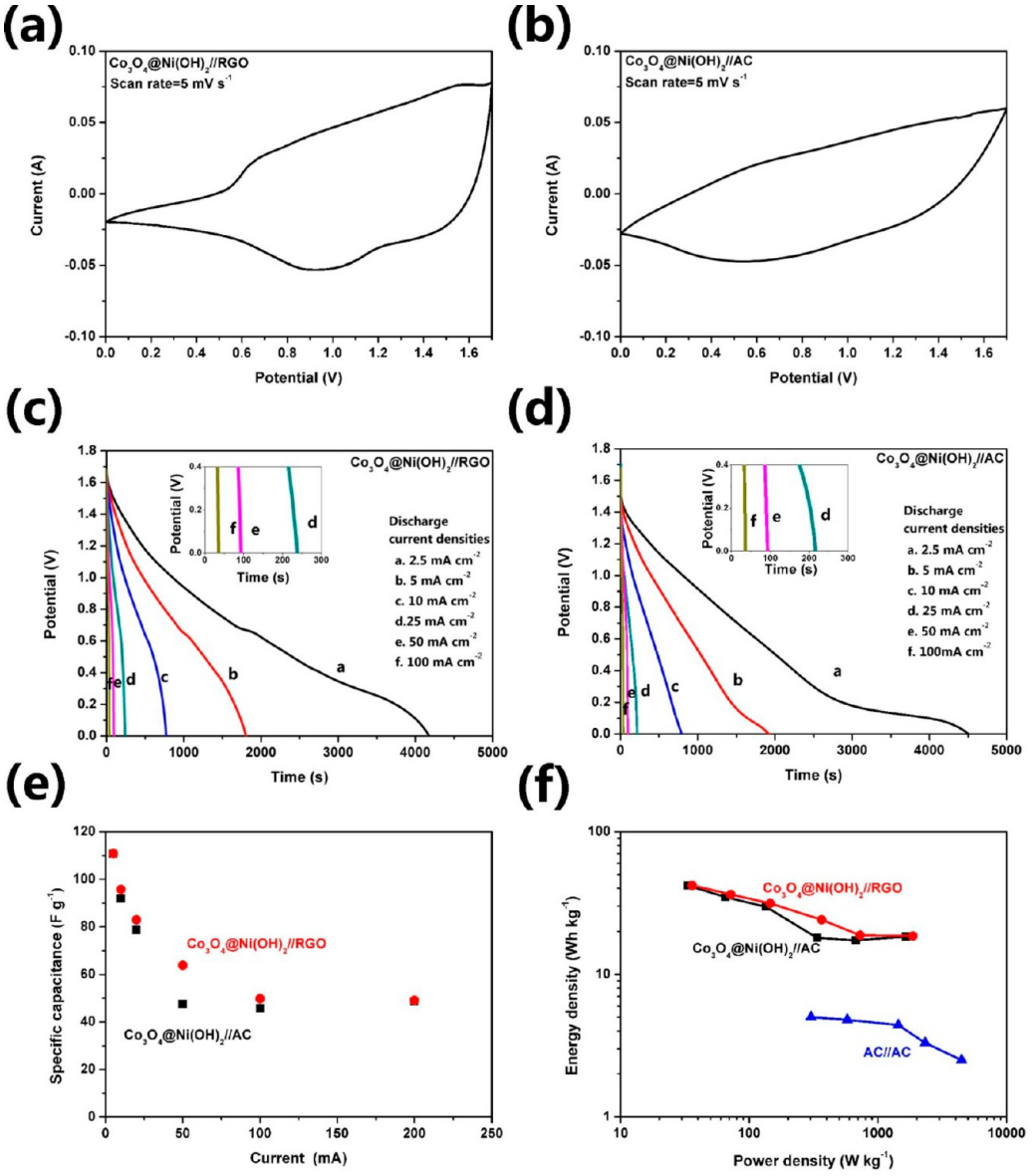

Figure 6. CV curves of Co_3O_4@$Ni(OH)_2$//RGO (a) and Co_3O_4@$Ni(OH)_2$//AC (b) asymmetric supercapacitors. Discharge curves of Co_3O_4@$Ni(OH)_2$//RGO (c) and Co_3O_4@$Ni(OH)_2$//AC (d) asymmetric supercapacitors at different current densities. Current dependence (e) and Ragone plot (f) of Co_3O_4@$Ni(OH)_2$//RGO and Co_3O_4@$Ni(OH)_2$//AC asymmetric supercapacitors.

The capacitive performances of the Co_3O_4@$Ni(OH)_2$//RGO and Co_3O_4@$Ni(OH)_2$//AC asymmetric supercapacitors are seen in Figure 6. Figure 6a,b show the CV curves of the Co_3O_4@$Ni(OH)_2$//RGO and Co_3O_4@$Ni(OH)_2$//AC at a scan rate of 5 mV s^{-1} with a potential window of 0 to 1.7 V in a KOH electrolyte. The asymmetric supercapacitors showed rectangle-like CV curves in a large potential range from 0 to 1.7 V, indicating a similar capacitive behavior as EDLCs and RuO_2.

To calculate the specific capacitances, energy densities, and power densities of these two asymmetric supercapacitors, galvanostatic discharge measurements at various charge−-discharge current densities were carried out. These discharge curves are shown in Figure 6c,d, and the charge−discharge curves of Co_3O_4@$Ni(OH)_2$//RGO are provided in the Supporting Information (Figure S5). All of these curves, belonging to the Co_3O_4@$Ni(OH)_2$//RGO and Co_3O_4@$Ni(OH)_2$//AC asymmetric supercapacitors, show a nearly linear variation with cell potential. This further indicates its capacitor-like behavior. The specific capacitances, energy densities, and power densities were calculated following the equations below

$$C_t = It/m_t\Delta V \tag{3}$$

$$E = \frac{1}{2m_t}C_t\Delta V^2 \tag{4}$$

$$P = \frac{I\Delta V}{2m_t} \tag{5}$$

where C_t (F g^{-1}) is the specific capacitance, E (Wh kg^{-1}) is the energy density, P (W kg^{-1}) is the power density, I (A) is the discharge current, t (s) is the discharge time, m (g) is the sum mass of Co_3O_4@$Ni(OH)_2$ and RGO (or AC), and ΔV (V) is the potential change during discharging. The total specific capacitances, which are calculated using the total mass of the active materials in both the anode and cathode, are indicated in

Figure 6e. The total specific capacitances of Co_3O_4@$Ni(OH)_2$//RGO at 2.5, 5, 12.5, 25, and 50 mA cm^{-2} are 110.8, 95.7, 83.0, 63.8, 49.7, and 49.0 F g^{-1}, respectively; those of Co_3O_4@$Ni(OH)_2$//AC are 110.6, 91.9, 78.8, 47.6, 45.8, and 48.6 F g^{-1}. It should be noted that the total specific capacitance, which is significantly enhanced by the ultrahigh pseudocapacitance of the Co_3O_4@$Ni(OH)_2$/NF electrode, is about 5-fold larger than the conventional AC-based symmetric capacitors (~20 F g^{-1}).[33] The corresponding energy density and power density at 2.5 mA cm^{-2} are 41.83 Wh kg^{-1} and 33.46 W kg^{-1} for Co_3O_4@$Ni(OH)_2$//AC and 41.90 Wh kg^{-1} and 36.10 W kg^{-1} for Co_3O_4@$Ni(OH)_2$//RGO, respectively. At a high discharge current density of 50 mA cm^{-2}, the energy density remained at 18.41 Wh kg^{-1} at a power density of 1661.05 W kg^{-1} for Co_3O_4@$Ni(OH)_2$//AC and 18.54 Wh kg^{-1} at 1869.60 W kg^{-1} for Co_3O_4@$Ni(OH)_2$//RGO, respectively. The superior energy density of our Co_3O_4@$Ni(OH)_2$/NF-based asymmetric supercapacitors can be attributed to their high specific capacitances. With such a high energy density and enhanced mass loading, our asymmetric supercapacitors demonstrated the ability to run a 3 V minifan and 2.5 V bulb (Figure 5c,d) even though the capacitance dimension is very small.

Figure 6f presents the Ragone plot (energy density vs power density) of our Co_3O_4@$Ni(OH)_2$//AC and Co_3O_4@$Ni(OH)_2$//RGO asymmetric supercapacitors as well as AC//AC symmetric supercapacitor. In view of this plot, at the same power density the Co_3O_4@$Ni(OH)_2$/NF-based asymmetric supercapacitors have much higher energy density than that of the AC//AC symmetric supercapacitor. (The information on the AC//AC symmetric supercapacitor is provided in the Supporting Information Figure S8.) The cycle stability of the Co_3O_4@$Ni(OH)_2$//RGO asymmetric supercapacitor is illustrated in Figure 7. The specific capacitance value first increased

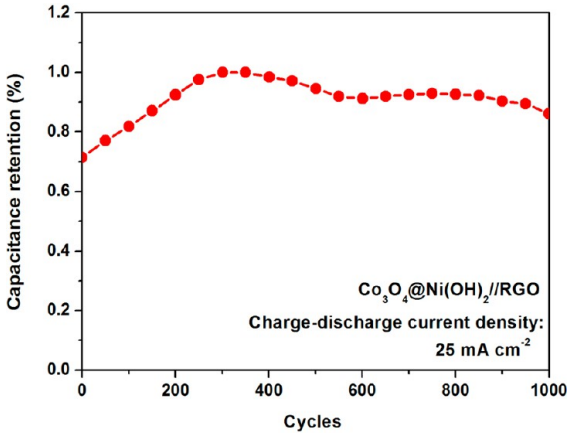

Figure 7. Cycle life test of the Co_3O_4@$Ni(OH)_2$//RGO asymmetric supercapacitor at a charge−discharge current density of 25 mA cm^{-2} for 1000 cycles.

in the initial 300 cycles because the electrode needed to be fully activated, similar to other group's observation.[11,34] Actually, Luo et al.[34] also found an increase in capacitance at the first 300 cycles for Mn−Ni−Co oxide composite electrode, and they claimed that it was caused by a gradual penetration of the electrolyte into the active materials. After the capacitance reached the maximum value, it started decreasing slowly. A total capacitance loss of only 14%, compared with the maximum value, was observed after the cell experienced 1000 cycles. It is noted that the capacitance value after 1000 cycles is even higher than the initial capacitance value. These superior capacitive behaviors of Co_3O_4@$Ni(OH)_2$/NF-based asymmetric supercapacitors considerably boost its application potential to replace traditional EDLCs in advanced energy-storage devices, even possibly finding applications in areas where Li-ion batteries are dominant.

4. CONCLUSIONS

A novel nanoarchitectured Co_3O_4@$Ni(OH)_2$ core−shell electrode with excellent pseudocapacitance behaviors has successfully been grown on a nickel foam collector by combining hydrothermal synthesis and chemical-bath deposition methods. The mass loading of the Co_3O_4@$Ni(OH)_2$ core−shell structure is very high (11.90 mg cm^{-2}). This high mass loading can increase the areal capacitance of the electrodes significantly. By combining the Co_3O_4@$Ni(OH)_2$/NF-based electrode with reduced graphene oxide (RGO) or active carbon (AC), we developed a series of Co_3O_4@$Ni(OH)_2$/NF-based asymmetric supercapacitors prototypes. These asymmetric supercapacitors exhibited superior performance, such as high specific capacitance and high energy density. Because of the large mass loading and high energy density, the prototype can drive a minifan or light a bulb even though its size is very small. These results indicate that our asymmetric supercapacitors have outstanding potential for commercial applications.

■ ASSOCIATED CONTENT

Ⓢ Supporting Information

Schematic and photograph of the formation progress of the electrode; XRD pattern of the precursor; charge−discharge curves of the Co_3O_4/NF, Co_3O_4@$Ni(OH)_2$/NF, and Co_3O_4@$Ni(OH)_2$//RGO; and electrochemical characterization of the AC and RGO single electrodes and the AC//AC symmetric supercapacitor. This material is available free of charge via the Internet at http://pubs.acs.org.

■ AUTHOR INFORMATION

Corresponding Author

*Tel: +65-65164632. Fax: +65 67763604. E-mail: msegongh@nus.edu.sg.

Notes

The authors declare no competing financial interest.

■ ACKNOWLEDGMENTS

Tang and Yin acknowledge support from a National University of Singapore (NUS) research scholarship.

■ REFERENCES

(1) Conway, B. E. *Electrochemical Supercapacitors: Scientific Fundamentals and Technological Applications*; Plenum Press: New York, 1999.
(2) Simon, P.; Gogotsi, Y. *Nat. Mater.* **2008**, *7*, 845−854.
(3) Miller, J. R.; Simon, P. *Science* **2008**, *321*, 651−652.
(4) Chen, Z.; Augustyn, V.; Wen, J.; Zhang, Y.; Shen, M.; Dunn, B.; Lu, Y. *Adv. Mat.* **2011**, *23*, 791−795.
(5) Bao, L.; Zang, J.; Li, X. *Nano Lett.* **2011**, *11*, 1215−1220.
(6) Chen, P.-C.; Shen, G.; Shi, Y.; Chen, H.; Zhou, C. *ACS Nano* **2010**, *4*, 4403−4411.
(7) Wang, G.; Zhang, L.; Zhang, J. *Chem. Soc. Rev.* **2012**, *41*, 797−828.

(8) Service, R. F. *Science* **2006**, *313*, 902.
(9) Tang, C.; Tang, Z.; Gong, H. *J. Electrochem. Soc.* **2012**, *159*, 651−656.
(10) Hu, G.; Tang, C.; Li, C.; Li, H.; Wang, Y.; Gong, H. *J. Electrochem. Soc.* **2011**, *158*, 695−699.
(11) Wei, T.-Y.; Chen, C.-H.; Chien, H.-C.; Lu, S.-Y.; Hu, C.-C. *Adv. Mater.* **2010**, *22*, 347−351.
(12) Kim, J.-H.; Zhu, K.; Yan, Y.; Perkins, C. L.; Frank, A. J. *Nano Lett.* **2010**, *10*, 4099−4104.
(13) Liu, J.; Jiang, J.; Cheng, C.; Li, H.; Zhang, J.; Gong, H.; Fan, H. J. *Adv. Mater.* **2011**, *23*, 2076−2081.
(14) Li, G. R.; Wang, Z. L.; Zheng, F. L.; Ou, Y. N.; Tong, Y. X. *J. Mater. Chem.* **2011**, *21*, 4217−4221.
(15) Zhang, H.; Yu, X.; Braun, P. V. *Nat. Nanotechnol.* **2011**, *6*, 277−281.
(16) Xu, J.; Wang, K.; Zu, S.-Z.; Han, B.-H.; Wei, Z. *ACS Nano* **2010**, *4*, 5019−5026.
(17) Hu, C.-C.; Chang, K.-H.; Lin, M.-C.; Wu, Y.-T. *Nano Lett.* **2006**, *6*, 2690−2695.
(18) Banerjee, P.; Perez, I.; Henn-Lecordier, L.; Lee, S. B.; Rubloff, G. W. *Nat. Nanotechnol.* **2009**, *4*, 292−296.
(19) Xia, X.; Tu, J.; Zhang, Y.; Wang, X.; Gu, C.; Zhao, X.-b.; Fan, H. J. *ACS Nano* **2012**, *6*, 5531−5538.
(20) Yuan, C.-Z.; Gao, B.; Zhang, X.-G. *J. Power Sources* **2007**, *173*, 606−612.
(21) Yoon, J. H.; Bang, H. J.; Prakash, J.; Sun, Y. K. *Mater. Chem. Phys.* **2008**, *110*, 222−227.
(22) Xue, Y.; Chen, Y.; Zhang, M.-L.; Yan, Y.-D. *Mater. Lett.* **2008**, *62*, 3884−3886.
(23) Wu, Z.-S.; Ren, W.; Wang, D.-W.; Li, F.; Liu, B.; Cheng, H.-M. *ACS Nano* **2010**, *4*, 5835−5842.
(24) Duffy, N. W.; Baldsing, W.; Pandolfo, A. G. *Electrochim. Acta* **2008**, *54*, 535−539.
(25) Wang, Y.-g.; Xia, Y.-y. *Electrochem. Comm.* **2005**, *7*, 1138−1142.
(26) Tang, Z.; Tang, C.-h.; Gong, H. *Adv. Funct. Mater.* **2012**, *22*, 1272−1278.
(27) Cao, L.; Xu, F.; Liang, Y. Y.; Li, H. L. *Adv. Mater.* **2004**, *16*, 1853−1857.
(28) Cao, C.-Y.; Guo, W.; Cui, Z.-M.; Song, W.-G.; Cai, W. *J. Mater. Chem.* **2011**, *21*, 3204−3209.
(29) Guan, C.; Liu, J.; Cheng, C.; Li, H.; Li, X.; Zhou, W.; Zhang, H.; Fan, H. J. *Energy Environ. Sci.* **2011**, *4*, 4496−4499.
(30) Liu, J.; Li, Y.; Huang, X.; Li, G.; Li, Z. *Adv. Funct. Mater.* **2008**, *18*, 1448−1458.
(31) Cao, L.; Kong, L.-B.; Liang, Y.-Y.; Li, H.-L. *Chem. Commun.* **2004**, 1646−1647.
(32) Zheng, J. P. *J. Electrochem. Soc.* **2003**, *150*, 484−492.
(33) Guo, Y.-G.; Hu, J.-S.; Wan, L.-J. *Adv. Mater.* **2008**, *20*, 2878−2887.
(34) Luo, J.-M.; Gao, B.; Zhang, X.-G. *Mater. Res. Bull.* **2008**, *43*, 1119−1125.
(35) Hu, G.; Li, C.; Gong, H. *J. Power Sources* **2010**, *195*, 6977−6981.